Available online at www.sciencedirect.com
ScienceDirect
Journal of Computational Physics 224 (2007) 1124–1144
JOURNAL OF COMPUTATIONAL PHYSICS
www.elsevier.com/locate/jcp

# An efficient and robust implicit operator for upwind point Gauss–Seidel method

Joo Sung Kim, Oh Joon Kwon *

*Department of Aerospace Engineering, Korea Advanced Institute of Science and Technology (KAIST), 373-1 Guseong-dong, Yuseong-gu, Daejeon 305-701, Republic of Korea*

Received 8 March 2006; received in revised form 26 September 2006; accepted 7 November 2006
Available online 15 December 2006

**Abstract**

An efficient and robust implicit operator for the point Gauss–Seidel method is presented for solving the compressible Euler equations. The new implicit operator was derived by adding a scalar form of artificial dissipation to the upwind implicit side. The amount of artificial dissipation was locally adjusted using a weighting factor based on the solution gradient. For validation, the performance of the new implicit operator was compared in detail with that of several existing implicit operators which have been widely used for solving the flow equations. Numerical experiments showed that the stability and convergence characteristics of the new implicit operator are significantly better than those of other existing implicit operators for calculating flows ranging from subsonic to hypersonic speeds.


*Keywords:* Implicit operator; Artificial dissipation model; Upwind point Gauss–Seidel; Euler equations; Stability and convergence

## 1. Introduction

Most of the implicit methods in computational fluid dynamics are derived by applying the local time linearization to the nonlinear flux terms [1], which can be evaluated using either central-difference schemes or upwind schemes. For central-difference schemes, it is necessary to add artificial dissipation to the explicit operator to suppress the odd–even decoupling and to control the numerical instability associated with the nonlinear discontinuities such as the shock wave. The artificial dissipation models are often described as a blending of second-difference and fourth-difference dissipation terms [2]. An artificial dissipation term is also added to the implicit operator to extend the stability limit imposed by the explicit artificial dissipation. The addition of the implicit artificial dissipation has a significant influence on the stability and convergence characteristics of central-difference implicit methods, even though it does not affect the spatial accuracy of the resultant steady-state solutions. The proper amount of implicit artificial dissipation to be added is closely related to that of the explicit artificial dissipation [3–5].

* Corresponding author. Tel.: +82 42 869 3720; fax: +82 42 869 3710.
*E-mail address:* ojkwon@kaist.ac.kr (O.J. Kwon).

0021-9991/$ - see front matter 
doi:10.1016/j.jcp.2006.11.008

Upwind schemes are dissipative in nature due to their differencing stencil, and thus additional dissipation is usually not needed. To obtain steady-state solutions, the consistency of adopting the same numerical splitting scheme for both implicit and explicit operators is not required, because the spatial accuracy of the solution is dictated solely by the explicit operator. In principle the numerical splitting scheme of the implicit operator needs to be selected such that the implicit method exhibits good stability and convergence characteristics [6,7]. Similar to the central-difference implicit methods, the performance of upwind implicit methods is also expected to be highly dependent on the dissipative property of the numerical splitting scheme adopted in the implicit operator, even though explicit control of the amount of the inherent numerical dissipation for upwind schemes is a difficult task.

Currently, several approximate inversion methods are available, including the alternating-direction implicit method [8], the point and line Gauss–Seidel (GS) methods [9], and the Krylov subspace method [10]. Among them, the point GS method has been widely used for unstructured mesh topologies [11–13], because it is algebraically simple and does not require any spatial coordinate direction splitting. Previous research works [14–17] showed that the performance of the point GS method is very sensitive to the dissipative property of the numerical splitting scheme of the implicit operator. When the splitting scheme of the implicit operator is more dissipative than that of the explicit operator, the point GS method leads to good stability characteristics, but typically yields slow convergence rates, as demonstrated by the lower–upper symmetric Gauss–Seidel (LU-SGS) method [15,16]. In this method, the implicit operator was based on the central-difference scheme with a scalar dissipation term which is typically more dissipative than the upwind scheme in the explicit operator. In contrast, when the dissipation level of the implicit operator is equal to that of the explicit operator, the stability can be severely restricted [17]. These observations clearly indicate that it is difficult to construct an efficient and robust implicit operator by adopting existing numerical splitting schemes with fixed level of numerical dissipation.

In the present study, a new implicit operator has been developed for the improvement of the efficiency and the robustness of the point GS method. For this purpose, an artificial dissipation model with an adjustable coefficient was incorporated in the upwind implicit side to flexibly control the dissipation level. Initially, the dependency of the stability characteristics on the dissipation level of the implicit operator was examined by applying the von Neumann stability analysis to a scalar model equation. Then assessment of the performance of existing implicit operators, which have been widely used for solving the Euler and Navier–Stokes equations, was made by testing the effect of their dissipation levels on the stability and convergence characteristics. Based on the insights from the analyses, an appropriate artificial dissipation model for the implicit operator of the point GS method was suggested. Finally, the benefits of using the artificial dissipation model in conjunction with upwind schemes were demonstrated through numerical experiments for flows ranging from subsonic to hypersonic speeds.

## 2. Implicit point Gauss–Seidel method

The two-dimensional compressible Euler equations under the ideal gas assumption may be written in an integral form for a control volume $\Omega$ with the boundary $\partial\Omega$:

$$\frac{\partial}{\partial t}\int_{\Omega} Q \, \mathrm{d}V + \oint_{\partial\Omega} f(Q) \, \mathrm{d}l = 0, \tag{1}$$

where $Q$ represents the vector of dependent variables, and $f(Q)$ is the inviscid flux vector. The governing equations were discretized using a node-based finite-volume method in which the variables were stored at the nodes of the mesh. The computational domain was divided into a finite number of triangles, and the control volumes were constructed from the median duals surrounding each node [11]. The application of the Euler implicit method and the local time linearization yields a linear system of equations:

$$\mathbf{L}\Delta Q^n = -\mathbf{R}, \tag{2}$$

where $\Delta Q^n = Q^{n+1} - Q^n$. $\mathbf{L}$ represents the implicit operator constructed with block matrices and has a dimension equal to the total number of nodes $N$. Also, $\mathbf{R}$ represents the explicit operator, which is a column vector with $N$ block entries. The explicit and implicit operators for the $i$th row are

$$\mathbf{R}_i = \sum_{j \in nf(i)} F_{ij}(Q_{\mathrm{L}}^n, Q_{\mathrm{R}}^n) l_{ij}, \tag{3}$$

$$\mathbf{L}_i = \frac{V_i}{\Delta t_i} I + \frac{\partial \mathbf{R}_i}{\partial Q}. \tag{4}$$

Here, $nf(i)$ is a set of face neighbor nodes for node $i$, and $l_{ij}$ is the length of the control volume boundary shared by nodes $i$ and $j$. Also, $V_i$ is the area of the control volume for node $i$. The local time step at node $i$, $\Delta t_i$, is determined from the definition of the Courant–Friedrichs–Lewy (CFL) number. $F_{ij}(Q_{\mathrm{L}}^n, Q_{\mathrm{R}}^n)$ is the numerical flux vector at the control volume boundary shared by nodes $i$ and $j$, and the subscripts L and R refer to the left and right states, respectively. The numerical flux of the explicit operator was evaluated in a second-order accurate manner using a linear reconstruction method, while the Jacobian $\partial \mathbf{R}_i/\partial Q$ for the implicit operator was approximated to first-order accuracy. This defect correction algorithm [18] has been commonly adopted in many implicit flow solvers, because the bandwidth can be reduced and the diagonal dominance property of the implicit operator is enhanced.

To obtain first-order accuracy, the flow variables at the left and right sides of the control volume boundary were set to those of the nodes at each side of the boundary. For second-order accuracy, the primitive variables were linearly extrapolated to the control volume boundary using a Taylor series expansion. The solution gradient required for the expansion was calculated using an unweighted least-square procedure [11]. This second-order approach is equivalent to a second-order, upwind-biased MUSCL differencing on Cartesian meshes [19]. In order to suppress the numerical oscillation of the solution associated with the reconstruction, Venkatakrishnan's limiter [20] was adopted.

The solution of the linear system of equations in Eq. (2) can be obtained by using a point Gauss–Seidel (GS) method in which several inner iterations with forward and backward sweeps are performed at each time step. The implicit matrix operator $\mathbf{L}$ may be split into three parts:

$$\mathbf{L} = \mathbf{D} + \mathbf{T}_1 + \mathbf{T}_2, \tag{5}$$

where $\mathbf{D}$ is the diagonal matrix, and $\mathbf{T}_1$ and $\mathbf{T}_2$ are the strictly lower and upper matrices, respectively. Then the point GS method can be written as the following two steps [21]:

$$[\mathbf{D} + \mathbf{T}_1]\Delta Q^* + [\mathbf{T}_2]\Delta Q^{k-1} = -\mathbf{R}, \tag{6}$$

$$[\mathbf{D} + \mathbf{T}_2]\Delta Q^k + [\mathbf{T}_1]\Delta Q^* = -\mathbf{R}. \tag{7}$$

The first equation corresponds to the forward sweep and the second one represents the backward sweep. The superscript $k$ ($k = 1, 2, 3, \ldots$) refers to the inner iteration index, and the superscript $*$ denotes the most recent values obtained from the forward sweep. The initial value $\Delta Q^0$ is taken to be zero.

Although the point GS method was originally developed for solving unfactored system of equations, it may also be expressed in a form equivalent to approximate factorization. Then the factorization error of the point GS method can be written as [21]

$$AF = [\mathbf{T}_1][\mathbf{D}]^{-1}[\mathbf{T}_2]\Delta Q^n. \tag{8}$$

The factorization error is known to be the main source of deteriorating the stability and convergence characteristics of approximate factorization methods, including the point GS method [21,22].

## 3. Analysis of point Gauss–Seidel method

In this section, the effect of the numerical dissipation level of the implicit operator on the performance of the point GS method was examined by applying the von Neumann stability analysis [5] to an idealized scalar model equation. In this stability analysis, the solution was decomposed into a Fourier series as $Q_{i,j}^n = E^n \mathrm{e}^{\mathrm{I}i\phi_x} \mathrm{e}^{\mathrm{I}j\phi_y}$ where $E^n$ is the error amplitude at time level $n$, and $\phi_x$ and $\phi_y$ are the $x$- and $y$-directional spatial frequencies, respectively. The magnitude of the largest eigenvalue of the amplification matrix defined by $G = E^{n+1}/E^n$ is the amplification factor and is denoted by $|G|$.

Consider a two-dimensional scalar convection equation

$$\frac{\partial}{\partial t} \int_\Omega u \, \mathrm{d}V + \oint_{\partial\Omega} f(u) \, \mathrm{d}l = 0, \tag{9}$$

where $f = (au\hat{i} + bu\hat{j}) \cdot \hat{n}$ and $\hat{n}$ refers to the unit normal vector pointing outward from the control volume boundary. The constants $a$ and $b$ are the wave speeds in the $x$ and $y$ directions, respectively. Opposite signs are assigned to the wave speeds (in the present study, $a > 0$ and $b < 0$) to account for the eigenvalues with mixed signs of the system of equations in Eq. (1). For the wave speeds with same signs, the factorization error always cancels out when the relaxation is performed in a symmetric manner, as done in the present study. This scalar equation was discretized using the Euler implicit method and the local time linearization as done in Eqs. (2)–(4). The spatial accuracy of the implicit operator was set to first order, and the explicit operator was obtained using a second-order, upwind-biased MUSCL scheme for the Cartesian meshes adopted in this stability analysis.

A generic form of upwind schemes may be written as

$$F_{i+1/2,j} = \frac{1}{2}[au_{\mathrm{L}} + au_{\mathrm{R}} - |a|(u_{\mathrm{R}} - u_{\mathrm{L}})]. \tag{10}$$

Then the first-order accuracy can be achieved by setting the state variables at the left and right sides of the control volume boundary as

$$u_{\mathrm{L}} = u_{i,j}, \quad u_{\mathrm{R}} = u_{i+1,j}. \tag{11}$$

The central-difference scheme with a second-difference artificial dissipation term can also be written in a form similar to that of upwind schemes:

$$F_{i+1/2,j} = \frac{1}{2}[au_{\mathrm{L}} + au_{\mathrm{R}} - \varepsilon_i|a|(u_{\mathrm{R}} - u_{\mathrm{L}})], \tag{12}$$

where $\varepsilon_i$ is the parameter which controls the amount of added dissipation.

In order to examine the effect of the numerical dissipation level of the implicit operator, the numerical flux of the implicit operator is modified by adding the second-difference artificial dissipation to the first-order upwind scheme:

$$F_{i+1/2,j} = \frac{1}{2}[au_{\mathrm{L}} + au_{\mathrm{R}} - (1+\varepsilon_i)|a|(u_{\mathrm{R}} - u_{\mathrm{L}})]. \tag{13}$$

Then the Jacobians for the implicit operator become

$$\begin{aligned} A^{+}_{i+1/2,j} &= \frac{\partial F_{i+1/2,j}}{\partial u_{\mathrm{L}}} = \frac{1}{2}[a + (1+\varepsilon_i)|a|], \\ A^{-}_{i+1/2,j} &= \frac{\partial F_{i+1/2,j}}{\partial u_{\mathrm{R}}} = \frac{1}{2}[a - (1+\varepsilon_i)|a|]. \end{aligned} \tag{14}$$

The numerical flux of the explicit operator is not changed, and thus the numerical flux of the implicit operator is more dissipative than that of the explicit operator when $\varepsilon_i > 0$. For $\varepsilon_i < 0$, an opposite statement can be made. When $\varepsilon_i = 0$, the levels of numerical dissipation in both operators are equal.

In Fig. 1, the maximum value of the amplification factor obtained over the entire spatial frequency spectrum is presented as a function of CFL number for selected values of $\varepsilon_i$. The results were obtained by performing single inner iteration for a flow angle, $\theta = b/a$, of $-10^{-2}$. The grid aspect ratio, $AR = \mathrm{d}x/\mathrm{d}y$, was set to unity since the Euler equations are typically calculated using meshes with nearly isotropic cells. Note that for a stable method, the value of the maximum amplification factor is unity, since the amplification factor at the lowest spatial frequency mode (i.e., $\phi_x = \phi_y = 0$ mode) is always unity.

When $\varepsilon_i = -0.5$, the point GS method becomes unstable for CFL numbers higher than unity. This limiting CFL number increases to approximately 10 when the dissipation levels in both operators are equal (i.e., $\varepsilon_i = 0$). As the dissipation level of the implicit operator further increases, the unstable behavior is rapidly alleviated, indicating that the stability characteristics of the point GS method can be improved by increasing the dissipation level of the implicit operator. However, with excessive dissipation, even though the method becomes unconditionally stable, the amplification factor approaches unity for all spatial frequencies and the convergence rate can deteriorate considerably. The results imply that the stability and convergence characteristics of the point GS method can be improved simultaneously only when the numerical dissipation level of the implicit operator is properly adjusted, presumably higher than that of the explicit operator. It was

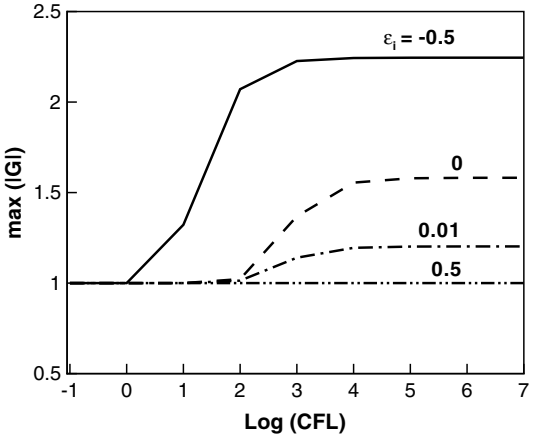


Fig. 1. Maximum amplification factor obtained over the entire spatial frequency spectrum as a function of CFL number for selected values of $\varepsilon_i$ (scalar equation).

observed that at other flow conditions with different flow angles or number of inner iterations, the essential features of the analysis were unchanged.

In principle, the convergence of the inner iteration procedure for the point GS method can be assured when the implicit operator is diagonally dominant. For first-order accurate upwind schemes, the diagonal dominance is always guaranteed for any time step size [23]. When the second-difference artificial dissipation is added to the upwind schemes, the ratio of the magnitude of the diagonal element to the sum of the magnitudes of the off-diagonal elements can be written as

$$1 + \frac{V_{i,j}/\Delta t_{i,j}}{2(1+\varepsilon_i)(a\,\mathrm{d}y - b\,\mathrm{d}x)}. \tag{15}$$

It shows that when the magnitude of $\varepsilon_i$ increases above zero, the diagonal dominance of the implicit operator is degraded and as a result the convergence rate of the inner-iteration procedure deteriorates. This indicates that for the efficiency and the robustness of the upwind point GS method, the added artificial dissipation should not be too large.

## 4. Existing implicit operators

Implicit operators can be obtained by applying the local time linearization to numerical fluxes. Consistent upwind (CU) implicit operators are constructed by adopting same upwind schemes for both explicit and implicit operators [1,15,16,24]. Alternatively, central-difference schemes can also be used in the implicit operator, while the explicit operator still employs an upwind scheme. For the central-difference schemes, the diagonal dominance property can be achieved only for a very small time step size, rendering the point GS method inefficient. Nevertheless, Jameson and Turkel [25] showed that a diagonally dominant central-difference implicit operator can still be constructed by adding numerical dissipation.

### 4.1. Construction of implicit operators

The upwind numerical flux vector based on Roe's flux-difference splitting (FDS) scheme [26] can be written at the control volume boundary shared by nodes $i$ and $j$ as

$$F_{ij} = \frac{1}{2}[f(Q_{\mathrm{L}}) + f(Q_{\mathrm{R}}) - |A(\tilde{Q})|(Q_{\mathrm{R}} - Q_{\mathrm{L}})], \tag{16}$$

where the flux Jacobian matrix $A$ is defined by $A = \partial f/\partial Q$. $\tilde{Q}$ represents the Roe-averaged values of the left and right states. Then the Jacobian matrices are obtained by linearizing the numerical flux in Eq. (16):

$$A_{ij}^{+} = \frac{1}{2}[A(Q_L) + |A(\tilde{Q})|], \quad A_{ij}^{-} = \frac{1}{2}[A(Q_R) - |A(\tilde{Q})|]. \tag{17}$$

In the linearization process, $|A(\tilde{Q})|$ is frozen in time [1].

The central-difference scheme with a second-difference scalar dissipation term can be written as

$$F_{ij} = \frac{1}{2}[f(Q_L) + f(Q_R) - k|\rho|(Q_R - Q_L)], \tag{18}$$

where $k$ is a constant to be specified and $|\rho|$ is the spectral radius of the flux Jacobian matrix. The Jacobian matrices of the Jameson–Turkel (JT) implicit operator are obtained by linearizing the central-difference scheme [27]:

$$A_{ij}^{+} = \frac{1}{2}[A(Q_L) + |\rho|\mathbf{I}], \quad A_{ij}^{-} = \frac{1}{2}[A(Q_R) - |\rho|\mathbf{I}], \tag{19}$$

where the constant $k$ is suppressed because it is typically set to unity.

Since the Euler equations are hyperbolic, the flux Jacobian matrix $A$ can be diagonalized. Then $|A|$ can be written as $|A| = P|\Lambda|P^{-1}$, where the columns of the matrix $P$ consist of the right eigenvectors of $A$. The diagonal matrix $|\Lambda|$ is given by $|\Lambda| = \mathrm{Diag}[|\lambda_1|, |\lambda_2|, |\lambda_3|, |\lambda_4|]$, where $\lambda_i$'s are the eigenvalues of $A$. Then the coefficient in the dissipation term of the central-difference scheme can be written as a linear combination of two matrices:

$$|\rho|\mathbf{I} = P|\rho|P^{-1} = |A| + A_{JT}, \tag{20}$$

where

$$A_{JT} = P\Lambda_{JT}P^{-1}, \tag{21}$$

$$\Lambda_{JT} = \mathrm{Diag}[|\rho| - |\lambda_1|, |\rho| - |\lambda_2|, |\rho| - |\lambda_3|, |\rho| - |\lambda_4|]. \tag{22}$$

It is clear that every element of $\Lambda_{JT}$ is greater than or equal to zero, because the spectral radius $|\rho|$ is defined by the largest eigenvalue of the matrix $A$. When the spectral radius is evaluated based on the Roe-averaged values, the Jacobian matrices of the JT implicit operator in Eq. (19) can be rewritten as

$$\begin{aligned} A_{ij}^{+} &= \frac{1}{2}[A(Q_L) + (|A(\tilde{Q})| + A_{JT}(\tilde{Q}))], \\ A_{ij}^{-} &= \frac{1}{2}[A(Q_R) - (|A(\tilde{Q})| + A_{JT}(\tilde{Q}))]. \end{aligned} \tag{23}$$

Compared to the upwind implicit operator based on Roe's FDS scheme in Eq. (17), the Jacobian matrices of the JT implicit operator contain an additional positive dissipation term. Thus, it is evident that the JT implicit operator is more dissipative than the upwind implicit operator.

### 4.2. Numerical experiments of existing implicit operators

The numerical behavior of the two implicit operators were examined through numerical experiments, with an emphasis on the effect of the numerical dissipation level of the operators. The selected test case was the flow over a solid bump described by $y = t\sin^2(\pi x)$ and located at $0 \leqslant x \leqslant 1$ [28]. For a fixed free stream Mach number of 0.8, two different flow problems, fully subsonic and transonic, were computed by changing the bump thickness $t$. The overall computational domain was 20 unit lengths long and 10 unit lengths high. The domain was decomposed into an unstructured triangular mesh composed of 6359 nodes, of which 215 lied on the bump surface. The slip boundary condition was imposed at the bottom boundary of the computational domain, including the bump. The characteristic boundary condition was applied to three other boundaries. In the explicit operator, Roe's FDS scheme was adopted.

In Fig. 2, the Mach number contours for 2% and 20% thick bumps are presented. It shows that the flow field of the 2% thick bump is completely subsonic, whereas for the 20% thick bump a strong shock wave exists at the leeward of the bump.

In Fig. 3, the convergence histories of the CU and JT implicit operators are compared for the bump flows. The convergence was measured by taking the logarithm of the $L_2$ norm of the residual of the conservation-of-

mass equation. In the beginning of the calculation, the CFL number was set to one for all test cases, and then increased inversely proportional to the reduction of the $L_2$ norm up to $10^7$ or until the maximum allowable value was reached. For the 2% thick bump flow, both CU and JT implicit operators were stable for all CFL numbers tested. However, the CU operator led to a much better convergence rate than the JT operator, indicating that addition of more dissipation to the implicit operator simply degrades the convergence behavior for fully subsonic flows.

In contrast, the results for the 20% thick bump flow revealed that the CU implicit operator is under a severe stability restriction, and the maximum allowable CFL number to obtain a machine-accurate solution was as low as three. However, the JT implicit operator did not suffer any stability restriction for all CFL numbers tested and led to a better convergence rate. The results of this 20% thick bump flow involving a strong shock wave indicated that the stability characteristics improve as the dissipation level of the implicit operator increases.

When the maximum CFL number was set to 30 for the flow over the 20% thick bump, the calculation using the CU implicit operator failed after 103 iterations. In Fig. 4, contours of the density residual are presented after 100 iterations, just before the calculation started to diverge. It clearly revealed that the region of significantly large residual values appears near the shock wave, indicating that the numerical instability of the CU implicit operator is intimately related to the presence of a strong solution gradient such as the shock wave. From the above stability and convergence results, it was found that the CU implicit operator in general has non-robust numerical behaviors, while the JT implicit operator is very robust but may lead to slow convergence. As a consequence of these results, it is highly desirable to devise a new implicit operator that is both efficient and robust for calculating flows involving strong solution gradients by properly adjusting the amount of added dissipation depending on the local flow characteristics.

## 5. Implicit operator with added artificial dissipation (AD)

It was shown that for the robustness of the point GS method, the numerical flux of the implicit operator needs to be more dissipative than that of the explicit operator. To achieve this feature, additional artificial dis-

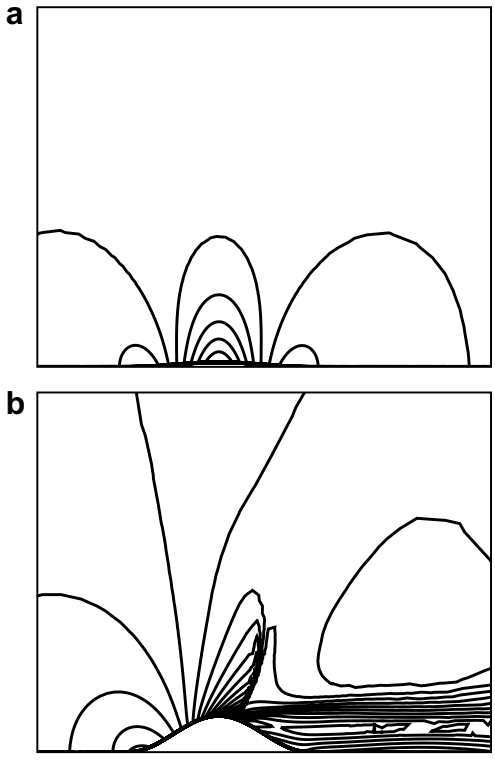


Fig. 2. Mach number contours over the bump: (a) 2% thickness and (b) 20% thickness.

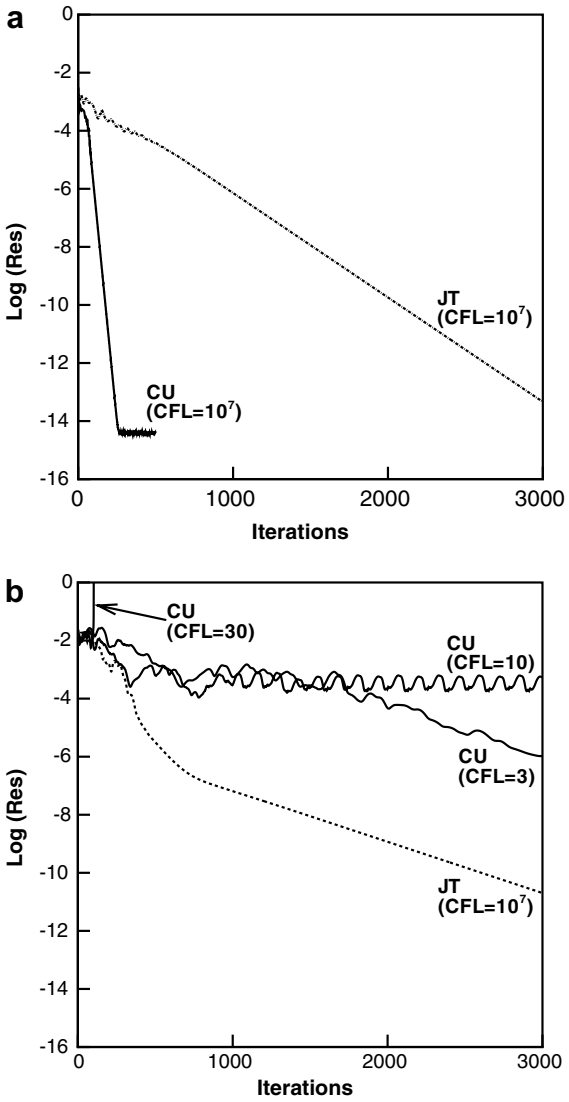


Fig. 3. Comparison of convergence histories between the CU and JT implicit operators for the bump flow: (a) 2% thickness and (b) 20% thickness.

sipation can be added to the implicit operator. The concept of adding artificial dissipation to the upwind implicit side was first attempted by Strang et al. [29] for the enhancement of the diagonal dominance. However, the addition of artificial dissipation in fact has an effect of deteriorating the diagonal dominance of the implicit operator, as shown in the previous section. In the present study, a second-difference artificial dissipation term was added to the upwind implicit side to increase the amount of dissipation of the implicit operator. Then the Jacobian matrices of the new implicit operator (AD) based on the numerical flux of Roe's FDS scheme can be written as

$$\begin{aligned} A_{ij}^{+} &= \frac{1}{2}[A(Q_{\mathrm{L}}) + (|A(\tilde{Q})| + \beta|\rho|)], \\ A_{ij}^{-} &= \frac{1}{2}[A(Q_{\mathrm{R}}) - (|A(\tilde{Q})| + \beta|\rho|)], \end{aligned} \tag{24}$$

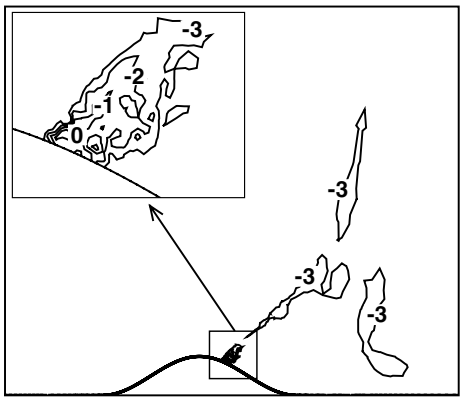


Fig. 4. Contours of the logarithm of the density residual just before the calculation started to diverge for the 20% thick bump flow.

where the coefficient $\beta$ is used to control the amount of added dissipation. Note that in the present AD implicit operator, a scalar form of artificial dissipation is added to the CU implicit operator, while the JT implicit operator in Eq. (23) has a matrix form.

To achieve fast convergence while maintaining good stability simultaneously, it is essential to choose $\beta$ properly. In the present study, $\beta$ was determined based on the von Neumann linear stability analysis such that the present AD implicit operator has the stability characteristics equivalent to those of the robust JT operator. For a demonstration purpose, the stability characteristics of the existing CU and JT operators were examined for the linearized constant coefficient Euler equations. The results were obtained at a Mach number of 0.3, and the flow angle, the grid aspect ratio, and the number of inner iteration were set equal to those used for the analysis of the scalar equation in Fig. 1. The CFL number was set to $10^7$. In the explicit operator, a second-order accurate upwind biased scheme was used. In Fig. 5, contours of the amplification factor of the CU and JT implicit operators are presented. It shows that while both implicit operators are unstable at low spatial frequencies, the maximum amplification factor of the JT implicit operator was still less than that of the CU operator, confirming that the JT operator is more robust than the CU operator.

In Fig. 6, the values of $\beta$ which yield the maximum amplification factor of the AD implicit operator equivalent to that of the JT operator are presented for various flow angles and Mach numbers. The flow angle changed from 0 to 1 in radian, and the local Mach number was tested between 0.2 and 5. The face Mach number $M_{\text{face}}$ was defined by the normal component of the local Mach number at the control volume face. The results were obtained for a fixed CFL number of $10^7$ by performing single inner iteration on an isotropic grid. From the results, it was found that the AD implicit operator has stability characteristics similar to or less than those of the JT operator, independent to the Mach number and the flow angle, when the coefficient $\beta$ is determined as a function of the face Mach number

$$\beta = \frac{b}{\max(1, M_{\text{face}})}, \tag{25}$$

where the value of $b$ is approximately 0.7.

In Fig. 7, contours of the amplification factor of the AD implicit operator are presented for the same flow condition in Fig. 5. It shows that the damping characteristics of the AD implicit operator are very similar to those of the JT operator in Fig. 5b over most of the spatial frequency spectrum, demonstrating that the stability and convergence characteristics of the AD implicit operator are very comparable to those of the JT operator.

In order to further improve the convergence characteristics of the AD implicit operator, the amount of added dissipation is adaptively adjusted depending on the flow characteristics. This technique is based on the observation that the instability of the CU implicit operator is mostly associated with large solution gradients such as the shock wave and thus the added dissipation is needed only in the local stiff flow regions. This adjustment can be made by imposing a weighting to the added dissipation based on the magnitude of the solution gradients, similar to the adaptive artificial dissipation for central-difference schemes [2]. An effective

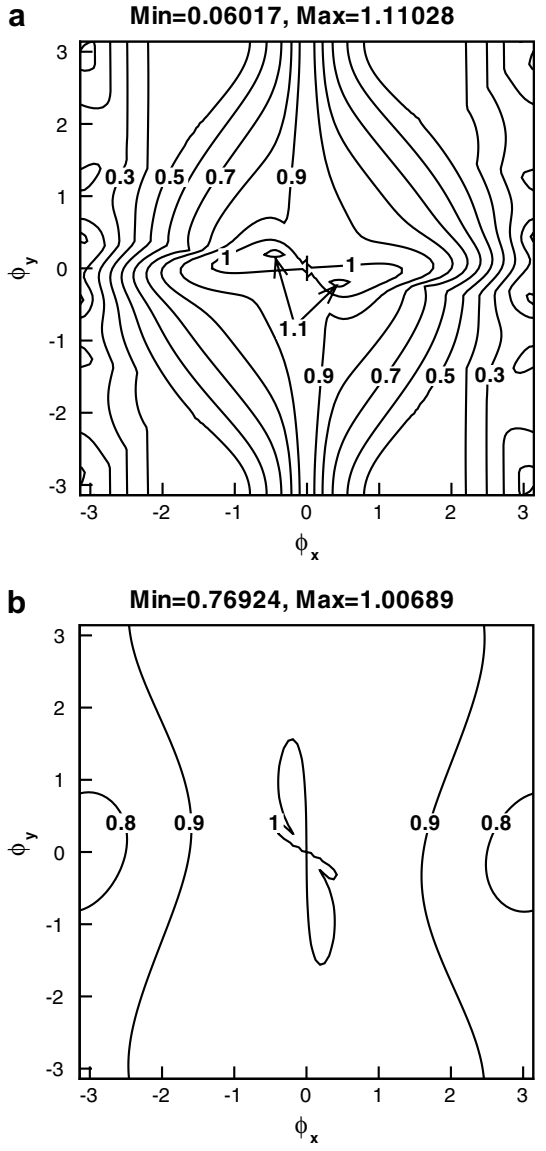


Fig. 5. Contours of the amplification factor: (a) CU implicit operator and (b) JT implicit operator.

choice of the weighting factor at the control volume face is the normalized second-difference of pressure [2], and for unstructured meshes this weighting factor can be evaluated using the undivided Laplacian of pressure [30]:

$$\tau_{ij} = \max(\tau_i, \tau_j), \tag{26}$$

$$\tau_i = \frac{|\sum_{k\in nf(i)}(p_k - p_i)|}{\sum_{k\in nf(i)}(p_k + p_i)}. \tag{27}$$

Then the AD implicit operator can be written as

$$\begin{aligned} A_{ij}^{+} &= \frac{1}{2}[A(Q_{\mathrm{L}}) + (|A(\tilde{Q})| + \tau\beta|\rho|)], \\ A_{ij}^{-} &= \frac{1}{2}[A(Q_{\mathrm{R}}) - (|A(\tilde{Q})| + \tau\beta|\rho|)]. \end{aligned} \tag{28}$$

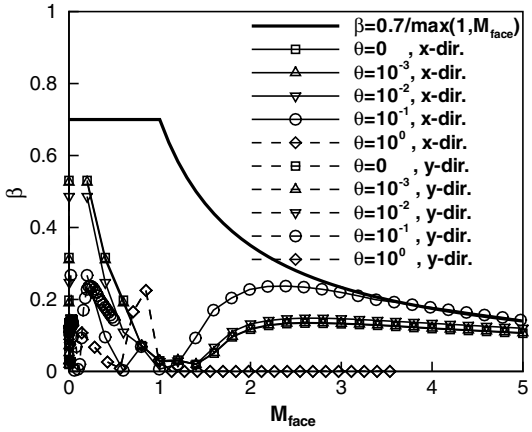


Fig. 6. Values of added dissipation coefficient $\beta$ needed for the AD implicit operator to yield the maximum amplification factor equivalent to that of the JT operator.

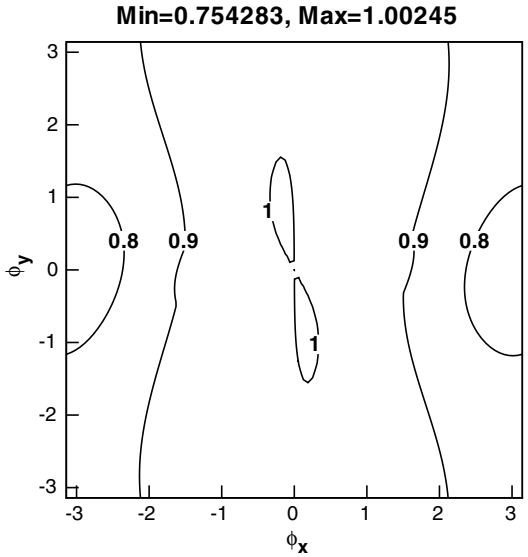


Fig. 7. Contours of the amplification factor of the AD implicit operator.

In the region of smooth flow, $\tau$ is proportional to the square of the cell size, and thus the effect of the added dissipation becomes negligible. When strong pressure gradients exist, the order of $\tau$ increases and the added dissipation works effectively for stabilizing the calculation. Here, the value of the constant $b$ in Eq. (25) needs to be adjusted properly because $\tau$ is not unity in the region where the added dissipation is in effect. For practical calculations of flows ranging from subsonic to hypersonic speeds, a reasonable value of $b$ is unity. This value was used for all numerical experiments presented in the next section. Adaptive control of the added dissipation also reduces the degradation of the diagonal dominance of the implicit operator, which is inevitably caused by the addition of the artificial dissipation to the upwind implicit operator as shown in Eq. (15).

For Cartesian meshes, when the velocity component normal to all control volume faces is supersonic, the CU implicit operator is not subject to any approximate factorization error. This is because either one of the lower matrix $\mathbf{T}_1$ or the upper matrix $\mathbf{T}_2$ in Eq. (8) becomes zero. In contrast, since the spectral radius is used in the coefficient of the dissipation term, the JT implicit operator does not have this favorable property. Even though this is true only for Cartesian meshes, the approximate factorization error of the CU implicit operator

is also expected to be smaller than that of the JT operator even on unstructured meshes. Since the present AD implicit operator is constructed such that the added dissipation becomes active locally in the neighborhood of stiff flow regions and it recovers to the CU implicit operator for the rest of the flow field, the magnitude of the approximate factorization error of the AD implicit operator is approximately equivalent to that of the CU operator.

The AD implicit operator can also be constructed for any other upwind numerical fluxes in a similar manner by adding the artificial dissipation to the corresponding Jacobian matrices.

## 6. Numerical results

Several compressible flows ranging from subsonic to hypersonic speeds were calculated to examine the stability and convergence characteristics of the three implicit operators for practical nonlinear problems. The numerical experiments about the effect of meshes with varying density were also conducted using solution-adaptive local mesh refinement based on the second derivative of density [31]. For the upwind differencing

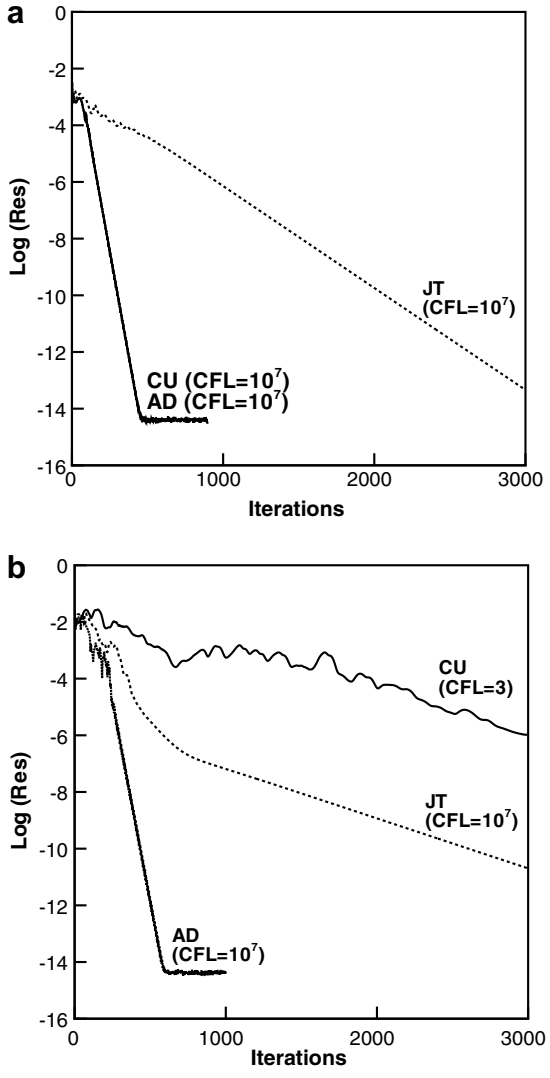


Fig. 8. Comparison of convergence histories of the three implicit operators for the bump flow: (a) 2% thickness and (b) 20% thickness.

of the nonlinear flux term, Roe's FDS scheme was mostly used, but van Leer's flux-vector splitting (FVS) scheme [32] was also tested to confirm the robustness of the present AD implicit operator. In these numerical experiments, the number of inner iterations was fixed to 10 for all test cases to maintain the consistency of the analysis, even though the implicit operators were not at the maximum performance. The CFL number ranged from 1 to $10^7$ and was increased inversely proportional to the reduction of the $L_2$ norm of the residual.

### 6.1. Bump flow

At first, the bump flow tested for the assessment of the performance of the existing operators was adopted again for numerical experiment. The convergence histories of the three implicit operators are compared in Fig. 8 for the maximum allowable CFL number of each operator above which the calculation simply diverges or enters into a limited cycle oscillation after a few orders of residual reduction. Even though the best convergence rate was obtained at a CFL number slightly lower than the maximum allowable CFL number [33], the convergence results are shown for the maximum allowable CFL number since the difference is relatively small.

For the 2% thick bump flow, the stability and convergence characteristics of the AD implicit operator were similar to those of the CU operator. Since the amount of dissipation added to the AD implicit operator was monitored by the magnitude of the pressure gradient, the numerical behavior of the AD implicit operator was evidently almost identical to that of the CU operator for this pure subsonic flow. It shows that all implicit operators considered were stable up to the largest CFL number tested, but the CU and AD implicit operators exhibited much better convergence rates than the JT operator.

For the 20% thick bump flow involving a strong shock wave, the CU implicit operator was subject to a severe restriction on the CFL number and led to a very slow convergence rate. However, the JT and AD implicit operators were unconditionally stable, demonstrating the effectiveness of adding numerical dissipation for

Table 1
Measure of relative CPU time required for the evaluation of each component

| Component | Normalized time |
|---|---|
| Explicit operator | 1.0 |
| CU implicit operator | 3.56 |
| JT implicit operator | 2.85 |
| AD implicit operator | 3.59 |
| GS sweeps | 14.0 |

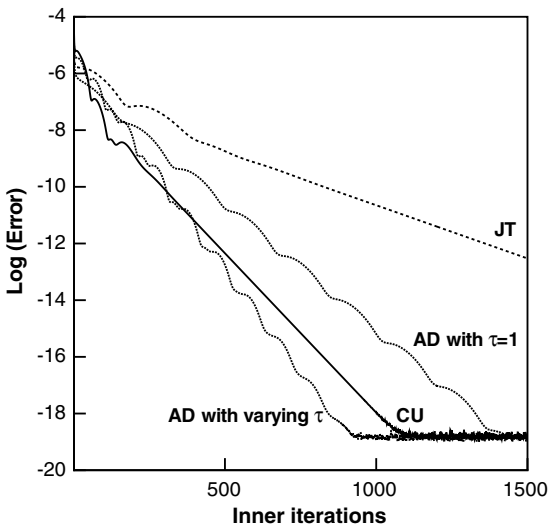


Fig. 9. Comparison of inner-iteration convergence histories of the three implicit operators for the 20% thick bump flow.

the improvement of the stability characteristics. Even though the two implicit operators showed similar stability characteristics, the AD implicit operator converged much faster than the JT operator.

In Table 1, the relative CPU time required for the evaluation of each component of the calculation is presented. The CPU time was measured on a PC with Pentium IV 2.4 GHz processor and was normalized by the cost for the explicit operator evaluation. It shows that the computational overhead for the evaluation of the added dissipation term in the present AD implicit operator was almost negligible compared to the overall

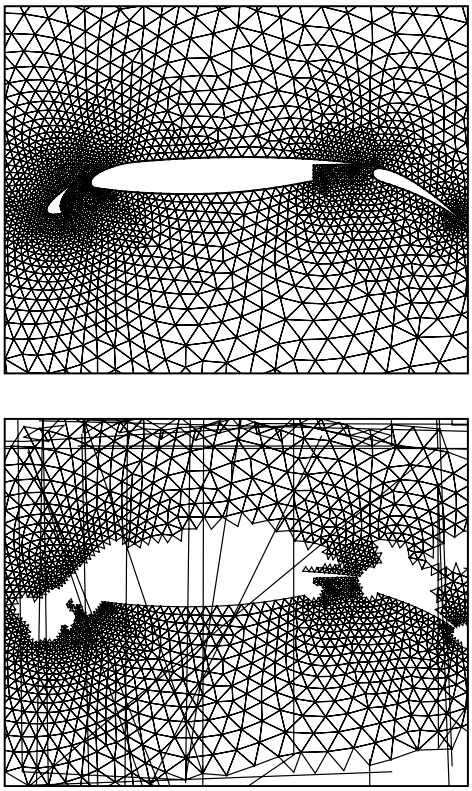

computational time. In the case of the subsonic flow, to achieve six orders of residual drop of the $L_2$ norm, the CU and AD implicit operators required 5582 and 5589 normalized CPU time, respectively, while it took 35,504 for the JT operator. For the transonic flow case, to reach the same level of residual drop, the AD implicit operator required 6581 normalized CPU time, but the JT and CU operators took 22,437 and 70,435, respectively.

To examine the effect of added artificial dissipation on the diagonal dominance property of the AD implicit operator, the inner-iteration convergence histories are compared for the 20% thick bump flow in Fig. 9. The convergence was measured by taking the logarithm of the $L_2$ norm of the error defined by $\Delta Q^k - \Delta Q^{k-1}$ where $k$ refers to the inner-iteration index. The result for each operator is shown for a CFL number of $10^7$ after restarting from the same intermediate solution obtained after 300 iterations using the AD implicit operator. The effect of the adaptive adjustment of the artificial dissipation in the AD implicit operator was also tested by comparing the results with those obtained by fixing the weighting factor to unity over the entire computational domain as done in [29]. It shows that uniformly added dissipation yielded a slower inner-iteration convergence

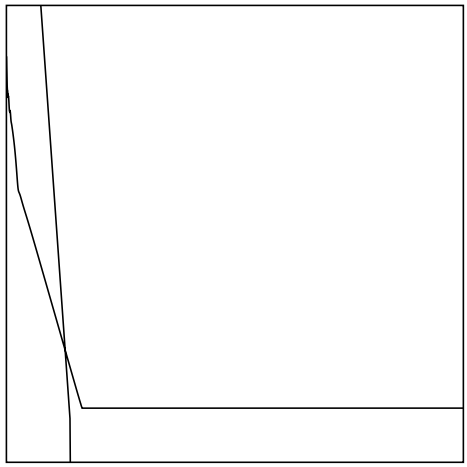

rate than the original CU operator, demonstrating that addition of the artificial dissipation in the upwind implicit operator deteriorates the diagonal dominance. In contrast, adaptive application of the artificial dissipation in the vicinity of the shock wave reduced the instability, and thus slightly improved the inner-iteration convergence behavior over the CU operator. The JT implicit operator led to the worst inner-iteration performance, presumably due to its excessively dissipative property.

In smooth flow regions, because the value of the weighting factor $\tau$ approaches zero, the CU and AD operators become almost identical, and thus the AD operator provides good damping characteristics over the JT operator for high frequency modes as shown for the CU operator in Fig. 5. This is a desirable property of a good smoother for multigrid schemes. Since the present AD implicit operator shows a much better convergence behavior than the other two operators for transonic flows, it is expected that the AD implicit operator also performs well as a smoother for multigrid schemes even in stiff flow regions.

### 6.2. Three-element airfoil flow

The second validation was made for a subsonic flow around the Douglas three-element airfoil at a free-stream Mach number of 0.2 and an angle of attack of 16.21°. Calculation started on an initial mesh consisted of 3015 nodes, of which 174 nodes were on the airfoil surface. To test the effect of mesh density, solution-adaptive mesh refinement by three levels was made, and the size of the final mesh increased to 12,984 nodes with 571 on the airfoil surface. The initial and final meshes in Fig. 10 show that the mesh refinement was made mainly around the airfoil surface and along the wakes emanating from the trailing edge of each element.

The calculated surface pressure distributions on the initial and refined meshes are compared with experimental data [34] in Fig. 11. It shows that the results obtained on the refined mesh generally compare better with the experiment than those of the initial mesh, even though the peak values near the leading edge of each element were slightly overpredicted, presumably due to the absence of the physical diffusion in the present calculation.

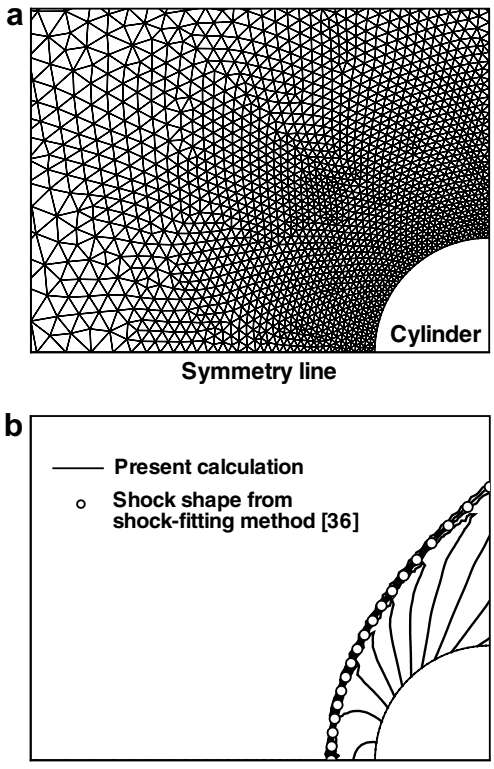


Fig. 13. Supersonic flow past a circular cylinder: (a) partial view of mesh (b) pressure contours at $M_\infty = 20$.

The convergence histories of the three implicit operators are compared in Fig. 12 on both initial and refined meshes for the maximum allowable CFL number of each implicit operator. The CU implicit operator showed a stable behavior on the initial mesh up to the largest CFL number tested, but became unstable for CFL numbers above $10^2$ on the refined mesh. In contrast, the JT and AD implicit operators exhibited an unconditionally stable behavior on both meshes. This behavior confirmed that the dissipation added in the JT and AD implicit operators is effective in increasing the stability limit even for subsonic flows. The dissipation adaptively adjusted based on the pressure gradient in the AD implicit operator worked well also for subsonic flows, leading to a much better convergence rate than the CU and JT operators, regardless of the mesh density.

### 6.3. Supersonic flow past a circular cylinder

The final validation was made for supersonic flows past a circular cylinder at freestream Mach numbers of 2, 5, 10, 15, and 20. For freestream Mach numbers higher than 10, the entropy correction function [35] was employed for both implicit and explicit operators to avoid the carbuncle problem of Roe's FDS scheme. The mesh used for the present calculations consisted of 2301 nodes, of which 34 lied on the cylinder surface. The computational domain was 5 unit lengths long and 10 unit lengths high. In Fig. 13, a partial view of the mesh and the pressure contours at a freestream Mach number of 20 are presented. It shows that the results of the present calculation agree well with the prediction by a shock-fitting method [36].

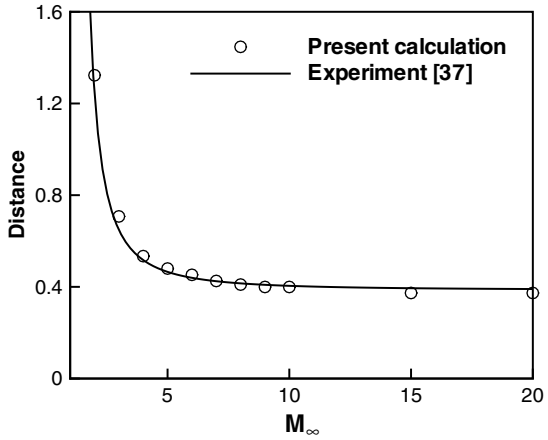


Fig. 14. Shock stand-off distance for supersonic flow past a circular cylinder.

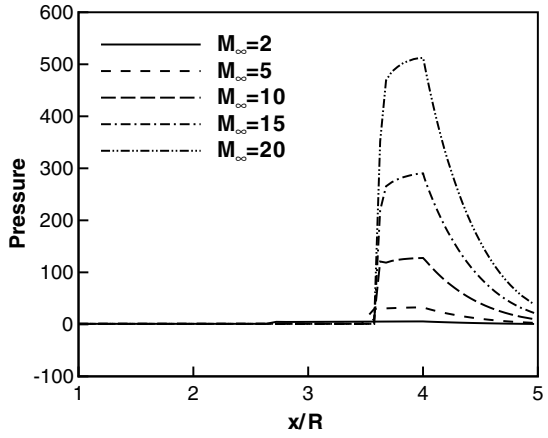


Fig. 15. Pressure distributions along the symmetry line and on the cylinder surface for supersonic flow past a circular cylinder.

In Fig. 14, the calculated shock stand-off distance from the surface of the circular cylinder is compared with experimental data [37]. It shows that the results of the present calculation obtained under the ideal gas assumption agree well with the experimental data. In Fig. 15, the pressure distributions along the symmetry line and on the cylinder surface are compared for all freestream Mach numbers considered. As the freestream Mach number becomes higher, the pressure ratio across the shock wave increases, leading to a large solution gradient.

In Table 2, a summary of the stability and convergence results is presented. Even though the CU implicit operator performed fairly well at $M_\infty = 2$, the stability and convergence characteristics rapidly degraded for higher Mach numbers and the maximum allowable CFL number was restricted below 10. This behavior agreed well with other numerical results [24] based on supersonic flows past a rounded cone calculated on structured meshes. For $M_\infty \geqslant 10$, unlike the subsonic and transonic flow cases, the JT implicit operator also

Table 2
Maximum allowable CFL number and the number of iterations required for six orders of residual drop for supersonic flow past a circular cylinder

| $M_\infty$ | CU | | JT | | AD | |
|---|---|---|---|---|---|---|
| | CFL | Iterations | CFL | Iterations | CFL | Iterations |
| 2 | $10^7$ | 223 | $10^7$ | 577 | $10^7$ | 280 |
| 5 | $10^1$ | 935 | $10^7$ | 514 | $10^7$ | 430 |
| 10 | 5 | 697 | 5 | 1280 | $10^7$ | 302 |
| 15 | 2 | 2032 | 3 | 1406 | $10^7$ | 271 |
| 20 | 2 | 1941 | 3 | 1423 | $10^7$ | 304 |

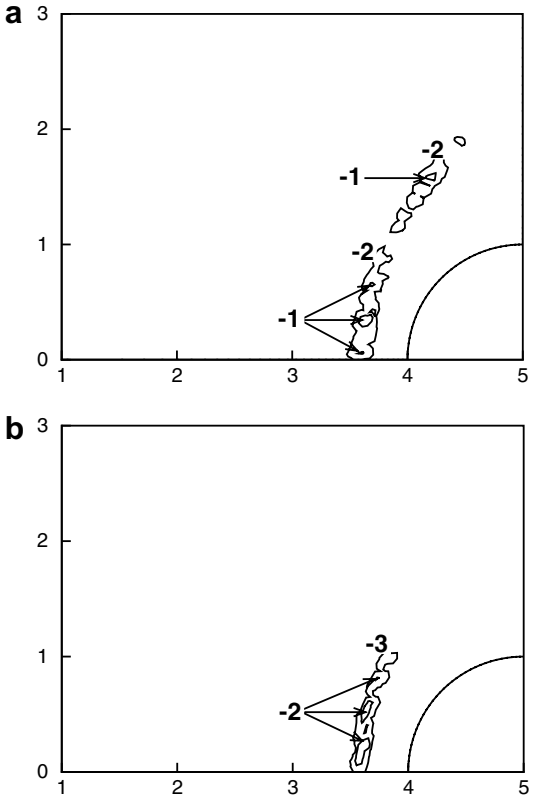


Fig. 16. Contours of the logarithm of the density residual for supersonic flow past a circular cylinder at $M_\infty = 20$: (a) CU implicit operator and (b) JT implicit operator.

experienced a severe stability restriction, and thus the convergence rate also became significantly poorer. However, the AD implicit operator with adaptive artificial dissipation was not subject to any instability for the complete range of CFL numbers tested and led to fast convergence rates for all Mach numbers considered. From these results, it can be stated that the scalar form of added dissipation employed in the AD implicit operator is more effective in alleviating the stability limit than the matrix form of the JT operator, particularly for high Mach number flows, even though the numerical behaviors of the two operators by the linear stability analysis were similar.

In the case of the CU and JT implicit operators, the calculations failed to converge to machine accuracy or diverged when the CFL number was set beyond the maximum allowable value depicted in Table 2. In Fig. 16, contours of the density residual by the CU and JT implicit operators are presented when the calculation failed to converge after a few orders of residual drop for a CFL number of 50. It shows that large residual and flow oscillation mostly exist along the shock wave. When the CFL number further increased, the oscillation was magnified and the calculation eventually diverged. However, the AD implicit operator was unconditionally stable for the complete range of CFL numbers tested.

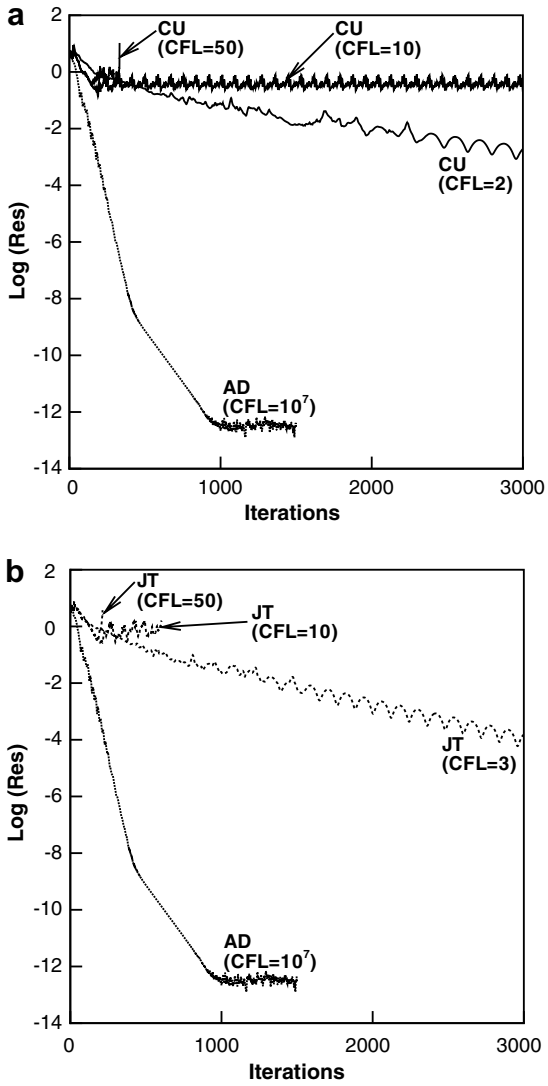


Fig. 17. Comparison of convergence histories on the refined mesh for supersonic flow past a circular cylinder at $M_\infty = 20$: (a) CU and AD implicit operators and (b) JT and AD implicit operators.

Table 3
Maximum allowable CFL number and the number of iterations required for six orders of residual drop for supersonic flow past a circular cylinder using van Leer's FVS scheme

| $M_\infty$ | CU | | JT | | AD | |
|---|---|---|---|---|---|---|
| | CFL | Iterations | CFL | Iterations | CFL | Iterations |
| 2 | $10^7$ | 205 | $10^7$ | 375 | $10^7$ | 215 |
| 5 | $10^7$ | 183 | $10^7$ | 234 | $10^7$ | 203 |
| 10 | $10^1$ | 388 | $10^1$ | 430 | $10^7$ | 201 |
| 15 | 5 | 884 | 5 | 958 | $10^7$ | 255 |
| 20 | 5 | 788 | 5 | 840 | $10^7$ | 291 |

In Fig. 17, the convergence histories on the adaptively refined mesh are presented at a freestream Mach number of 20. The mesh refinement was made mostly along the shock wave and the number of nodes increased to 3251. The results show that the numerical instabilities of the CU and JT implicit operators further amplified on the refined mesh, and the calculations diverged even for very low CFL numbers where on the coarse initial mesh only convergence stall was observed. The AD implicit operator, however, did not show any indication of stability restriction up to the largest CFL number tested and converged very fast on the refined mesh.

The stability and convergence characteristics of the three implicit operators were also tested by adopting van Leer's FVS scheme in the explicit operator, and the results are presented in Table 3. In these calculations, the CU and AD operators were also constructed based on the same FVS scheme. It shows that the AD implicit operator was not subject to any instability and consistently led to good convergence rates at all Mach numbers, while the other two implicit operators were under severe stability restrictions at high freestream Mach numbers, similar to those cases with Roe's FDS scheme. Thus it is believed that the present adaptive dissipation model proposed to improve the stability and convergence characteristics of the point GS method also works well with other upwind schemes as well.

## 7. Conclusions

In the present study, an efficient and robust implicit operator for the upwind point Gauss–Seidel method has been developed for solving the compressible Euler equations. It was found that the amount of numerical dissipation in the implicit operator has a significant effect on the stability and convergence characteristics. For the robustness of the point Gauss–Seidel method, the numerical flux of the implicit operator needs to be more dissipative than that of the explicit operator. Also, the amount of numerical dissipation in the implicit operator should be determined carefully to achieve the efficiency and the robustness simultaneously. Based on these observations, a new scalar form of adaptive artificial dissipation model was developed for upwind implicit operators.

In order to validate the implicit operator with the new dissipation model, numerical experiments were conducted for flows ranging from subsonic to hypersonic speeds. For subsonic and transonic flow problems, both matrix and scalar forms of added dissipation worked well for improving the numerical stability, and the Jameson–Turkel operator and the present operator were unconditionally stable. Even though the two implicit operators had similar stability characteristics, the present operator always showed much better convergence rates than the Jameson–Turkel operator. For hypersonic flow problems, it was found that the matrix form of added dissipation was not robust enough for handling strong shock waves, and thus the Jameson–Turkel implicit operator suffered severe convergence degradation. Meanwhile the present implicit operator always showed good stability and convergence characteristics. It was concluded that the present implicit operator with a scalar form of adaptive artificial dissipation is more efficient and robust than other existing implicit operators for solving the compressible Euler equations over a wide range of flow problems.

## References

[1] T.J. Barth, Analysis of implicit local linearization techniques for upwind and TVD algorithms, AIAA Paper87-0595, 1987.
[2] A. Jameson, W. Schmidt, E. Turkel, Numerical solutions of the Euler equations by finite volume methods using Runge–Kutta time-stepping schemes, AIAA Paper 81-1259, 1981.

[3] T.H. Pulliam, J.L. Steger, Implicit finite-difference simulations of three-dimensional compressible flow, AIAA J. 18 (2) (1978) 159–167.
[4] A. Jameson, S. Yoon, Multigrid solution of the Euler equations using implicit schemes, AIAA J. 24 (11) (1986) 1737–1743.
[5] T.H. Pulliam, Artificial dissipation models for the Euler equations, AIAA J. 24 (12) (1986) 1931–1940.
[6] M.S. Liou, B. van Leer, Choice of implicit and explicit operators for the upwind differencing method, AIAA Paper 88-0624, 1988.
[7] J.R. Amaladas, H. Kamath, Implicit and multigrid procedures for steady-state computations with upwind algorithms, Comput. Fluids 28 (1999) 187–212.
[8] R.M. Beam, R.F. Warming, An implicit factored scheme for the compressible Navier–Stokes equations, AIAA J. 16 (4) (1978) 393–402.
[9] S.R. Chakravarthy, Relaxation methods for unfactored implicit upwind schemes, AIAA Paper 84-0165, 1984.
[10] Y. Saad, M.H. Schultz, GMRES: a generalized minimal residual algorithm for solving nonsymmetric linear systems, J. Sci. Stat. Comput. 7 (3) (1986) 856–869.
[11] W.K. Anderson, D.L. Bonhaus, An implicit upwind algorithm for computing turbulent flows on unstructured grids, Comput. Fluids 23 (1) (1994) 1–21.
[12] N.T. Frink, Assessment of an unstructured-grid method for predicting 3-d turbulent viscous flows, AIAA Paper 96-0292, 1996.
[13] W.S. Oh, J.S. Kim, O.J. Kwon, Numerical simulation of two-dimensional blade–vortex interactions using unstructured adaptive meshes, AIAA J. 40 (3) (2002) 474–480.
[14] S. Yoon, A. Jameson, Lower-upper symmetric-Gauss–Seidel method for the Euler and Navier–Stokes equations, AIAA J. 26 (9) (1988) 1025–1026.
[15] M.J. Wright, G.V. Candler, M. Prampolini, Data-parallel lower–upper relaxation method for the Navier–Stokes equations, AIAA J. 34 (7) (1996) 1371–1377.
[16] R.F. Chen, Z.J. Wang, Fast, block lower–upper symmetric Gauss–Seidel scheme for arbitrary grids, AIAA J. 38 (12) (2000) 2238–2245.
[17] D.L. Whitfield, L.K. Taylor, Discretized Newton-relaxation solution of high resolution flux-difference split schemes, AIAA Paper 91-1539, 1991.
[18] B. Koren, Defect correction and multigrid for an efficient and accurate computation of airfoil flows, J. Comput. Phys. 77 (1988) 183–206.
[19] W.K. Anderson, J.L. Thomas, B. van Leer, Comparison of finite volume flux vector splittings for the Euler equations, AIAA J. 24 (9) (1986) 1453–1460.
[20] V. Venkatakrishnan, Convergence to steady state solutions of the Euler equations on unstructured grids with limiters, J. Comput. Phys. 118 (1995) 120–130.
[21] P.E.O. Buelow, S. Venkateswaran, C.L. Merkle, Stability and convergence analysis of implicit upwind schemes, Comput. Fluids 30 (2001) 961–988.
[22] R.W. MacCormack, T.H. Pulliam, Assessment of a new numerical procedure for fluid dynamics, AIAA Paper 98-2821, 1998.
[23] A.C. Taylor III, W.-F. Ng, R.W. Walters, Upwind relaxation methods for the Navier–Stokes equations using inner iterations, J. Comput. Phys. 99 (1992) 68–78.
[24] L. Mottura, L. Vigevano, M. Zaccanti, Factorized implicit upwind methods applied to inviscid flows at high Mach number, AIAA Paper 98-2822, 1998.
[25] A. Jameson, E. Turkel, Implicit schemes and LU decompositions, Math. Comput. 37 (156) (1981) 385–397.
[26] P.L. Roe, Approximate Riemann solvers, parameter vectors, and difference schemes, J. Comput. Phys. 43 (1981) 357–372.
[27] H. Luo, J.D. Baum, R. Löhner, A fast, matrix-free implicit method for compressible flows on unstructured grids, J. Comput. Phys. 146 (1998) 664–690.
[28] D.L. Darmofal, K. Sui, A robust multigrid algorithm for the Euler equations with local preconditioning and semi-coarsening, J. Comput. Phys. 151 (1999) 728–756.
[29] W.Z. Strang, R.F. Tomaro, M.J. Grismer, The defining methods of *Cobalt*$_{60}$: a parallel, implicit, unstructured Euler/Navier–Stokes flow solver, AIAA Paper 99-0786, 1999.
[30] D.J. Mavriplis, A. Jameson, Multigrid solution of the Navier–Stokes equations on triangular meshes, AIAA J. 28 (8) (1990) 1415–1425.
[31] D.L. De Zeeuw, A quadtree-based adaptively-refined Cartesian-grid algorithm for solution of the Euler equations, Ph.D. Thesis, University of Michigan, 1993.
[32] B. van Leer, Flux-vector splitting for the Euler equations, Lect. Notes Phys. 170 (1982) 507–512.
[33] W.K. Anderson, R.D. Rausch, D.L. Bonhaus, Implicit/multigrid algorithms for incompressible turbulent flows on unstructured grids, J. Comput. Phys. 128 (1996) 391–408.
[34] W.O. Valarezo, C.J. Dominik, R.J. McGhee, W.L. Goodman, K.B. Paschal, Multi-element airfoil optimization for maximum lift at high Reynolds numbers, AIAA Paper 91-3332, 1991.
[35] H.C. Yee, G.H. Klopfer, J.-L. Montagne, High-resolution shock-capturing schemes for inviscid and viscous hypersonic flows, J. Comput. Phys. 88 (1990) 31–61.
[36] A.N. Lyubimov, V.V. Rusanov, Gas flows past blunt bodies, NASA TT-F 715, 1973.
[37] F.S. Billing, Shock-wave shapes around spherical- and cylindrical-nosed bodies, J. Spacecraft 4 (6) (1967) 822–823.